Accepted Manuscript

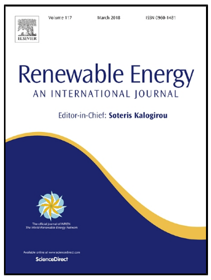

Cyclic Thermal Performance Analysis of a Traditional Single-Layered and of a Novel Multi-Layered Packed-Bed Molten Salt Thermocline Tank

Meng-Jie Li, Yu Qiu, Ming-Jia Li

PII:	S0960-1481(17)31139-4
DOI:	10.1016/j.renene.2017.11.038
Reference:	RENE 9440
To appear in:	*Renewable Energy*
Received Date:	30 May 2017
Revised Date:	21 October 2017
Accepted Date:	13 November 2017

Please cite this article as: Meng-Jie Li, Yu Qiu, Ming-Jia Li, Cyclic Thermal Performance Analysis of a Traditional Single-Layered and of a Novel Multi-Layered Packed-Bed Molten Salt Thermocline Tank, *Renewable Energy* (2017), doi: 10.1016/j.renene.2017.11.038

HIGHLIGHTS

- Cyclic thermal performance of packed-bed thermocline tank is analyzed.
- Effects of thermocline on performance of thermocline tank are illustrated.
- The expanding and shortening effects on thermocline thickness are first reported.
- A novel multi-layered packed-bed molten salt thermocline tank is proposed.
- Great rise in useful energy and small drop in efficiency of novel tank are revealed.

Cyclic Thermal Performance Analysis of a Traditional Single-Layered and of a Novel Multi-Layered Packed-Bed Molten Salt Thermocline Tank

Meng-Jie Li, Yu Qiu, Ming-Jia Li*

(Key Laboratory of Thermo-Fluid Science and Engineering of Ministry of Education, School of Energy and Power Engineering, Xi'an Jiaotong University, Xi'an, Shaanxi, 710049, China)

(Corresponding author: E-mail: mjli1990@xjtu.edu.cn)

Abstract: In the study, a transient, two-dimensional and axisymmetric model of the packed-bed thermocline tank is developed. Based on the model, the cyclic thermal performance of a traditional Single-Layered and of a novel Multi-Layered Packed-Bed molten salt Thermocline Tank (SLPBTT, MLPBTT) are analyzed. First, the analysis of cyclic thermal performance of SLPBTT shows the performance can be enhanced by reducing the retention thermocline thickness. Second, this is the first time for a detailed investigation of the expanding and the shortening effects on thermocline thickness at the interface between two kinds of filler. In addition, a novel MLPBTT is designed utilizing the above interface effects for improving the performance by controlling thermocline expansion. Finally, the studies on the performance of MLPBTTs adopting three fillers (quartzite rock, cast iron, and high-temperature concrete) with different heights present that the useful energy can be increased while thermal efficiency will be reduced with the increasing cast iron's height. An optimized MLPBTT shows a significant improvement in the useful energy of 10.5% and a small drop in thermal efficiency of 2.1 % in discharging process compared with those of SLPBTT using the quartzite rock. The results can be beneficial for the design and optimization of PBTT.

Keywords: *Packed-bed; Thermocline; Thermal energy storage; Solar energy; Cyclic process; Novel multi-layered packed-bed*

1. Introduction

The excessive usage of fossil fuel aggravates the environmental pollution and imposes negative effects on a social economy. Therefore, it becomes an important task to encourage the development of renewable energy resource for all countries [1-4]. Solar energy is a clean alternative energy source that is abundant and widely available. The efficient utilization of solar energy is being considered as a promising solution to the environmental issues [5-7]. The Concentrating Solar Power (CSP) converts the concentrated solar thermal energy into electricity with high efficiency and low cost. Thus, the CSP generation technology has become a promising approach to utilize solar energy [8-12].

The Thermal energy storage (TES) system has attracted an increasing attention during recent years in the CSP. It is one of the most important subsystems in the CSP because it can maintain a relatively steady power output, and drive the system constantly [13-20]. The TES system can be divided into the two-tank system and the one-tank thermocline system. The two-tank system, which is the most mature technology, stores thermal energy by using the molten salt in a hot tank and a cold tank. In the one-tank system, both high-price molten salt and low-cost solid filler are adopted as thermal storage materials. There is a large-temperature-gradient region called thermocline, which segregates the high-temperature salt and low-temperature salt in a single tank during the charging process or discharging process [21]. The Packed-Bed Thermocline Tank system (PBTT) has attracted increasing attention during the past few years because less salt is needed, and the cost of TES can be reduced by 30-37% compared with that of the two-tank system [22].

Many experimental and numerical investigations focus on the thermal performance of PBTT. In the respect of experimental studies, Pacheco and Showalter et al. [23] set up a pilot (2.3MWht) molten salt packed-bed thermocline tank in the Sandia National Laboratories in 2002. Quartzite rock and sands were used as the low-cost filler, and a eutectic salt called Solar Salt (60wt%$NaNO_3$, 40wt%KNO_3) was adopted as the Heat Transfer Fluid (HTF). This work successfully demonstrated that the PBTT was a viable thermal storage technology. Okello et al. [24-26] developed the PBTT combination system composing sensible storage subsystems and latent thermal storage subsystems in which the air was used as HTF. The results suggested that the stored thermal energy of tank can be improved when phase change material cylinders were added into the quartzite rock packed-bed. Zanganeh et al. [27] built a 6.5MWht pilot-scale thermal storage unit immersed in the ground in which a packed bed of rocks was as storing material and the air was as HTF. It experimentally demonstrated to generate thermocline. Other experiments of PBTT using air, oil, and water as the HTF were studied in recent years, including Li et al.[28] Bruch et al.[29], Vaivudh et al[30], and Grirate et al[31]. In the respect of the numerical studies, Xu et al. [32, 33] compared the effects of different correlations of effective thermal conductivity and interstitial heat transfer coefficient on thermal performance prediction. Authors further studied the effect of the filler properties such as filler diameter and filler materials on the heat transfer characteristic between filler and salt. It had been proved that a thermocline region will be retained near the exit, which is called the retention thermocline region when a charging process or discharging process ends. Bayón et al. [34] analyzed the effect of the retention thermocline on the thermal performance of the thermocline tank. It was found that a lot of thermal energy cannot be utilized, which results in a negative effect on the performance of thermal storage. Moreover, the results suggested that extracting thermocline can improve the efficiency of the tank with some negative impacts on steam generations and solar fields [35]. Some numerical studies also focused on the performance of the thermocline tank by adopting the phase change material (PCM) as part of the storage media. It was found that the effective discharging energy of the tank increased and it was more cost-competitive than the two tanks TES because of the PCM's high energy storage density during the phase change process [21 ,48].

From the literature review, it can be concluded that great efforts have been focused on the following aspects to improve the thermal performance [36-41] including the investigation of the thermal performance of PBTT using different HTFs, the optimization of filler materials and the operation strategies of PBTT. Although the thermocline has negative effects on the thermal performance, it is still a significant issue that has been analyzed frequently. However, only a few studies focus on improving the thermal performance of PBTT by controlling the development of thermocline so far.

The objectives of work are to study the cyclic thermal performance of a Single-Layered and of a novel Multi-Layered Packed-Bed Molten Salt Thermocline Tank (SLPBTT, MLPBTT) , and further to improve the performance of MLPBTT by controlling the thermocline explosion. A numerical model is developed to simulate the charging and discharging processes. Based on the model, the cyclic thermal performance of SLPBTT and the effects of thermocline explosion on the performance are firstly analyzed. Then, detailed information of the thermocline interface effect is reported for the first time, and an MLPBTT is proposed to control the thermocline explosion by utilizing the interface effect. Finally, after comparing the cyclic thermal performance and capital costs of several MLPBTTs, some suggestions of MLPBTT design are provided to guide the design and performance optimization of PBTT.

2. Model description

2.1 Physical model

In the paper, the packed-bed thermocline tanks are adopted to analyze the cyclic thermal performance of the tank and the effects of thermocline on performance. The packed-bed thermocline tanks include a traditional SLPBTT and a novel MLPBTT. The quartzite rock is treated as the filler in the SLPBTT, and several different fillers are adopted in the novel MLPBTT. The sketches of SLPBTT and MLPBTT are shown in Fig. 1 and Fig. 2, respectively.

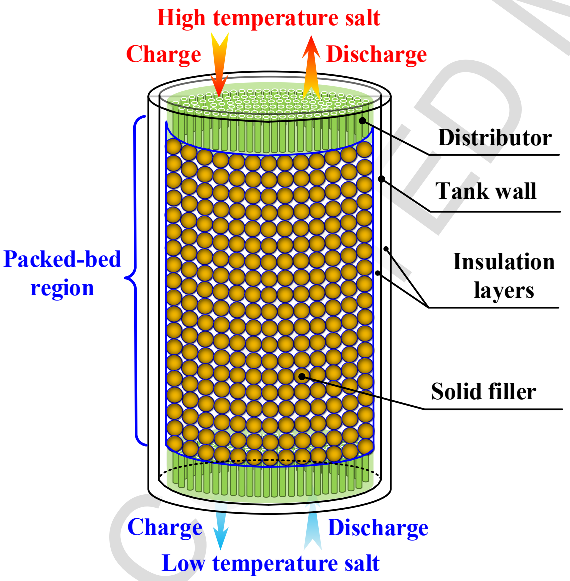

Fig. 1. Sketch of a traditional Single-Layered Packed-Bed Thermocline Tank (SLPBTT).

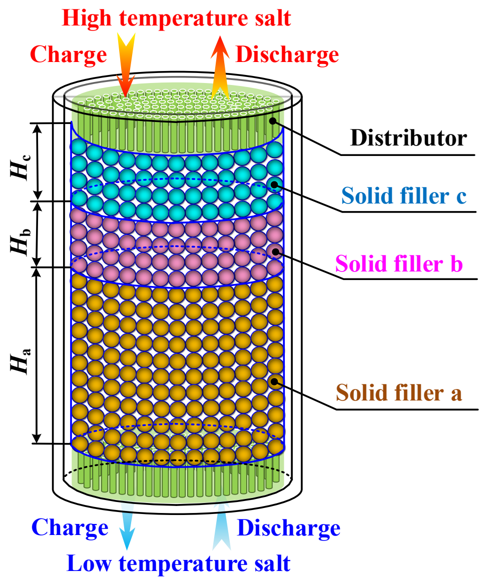

Fig. 2. Sketch of a novel Multi-Layered Packed-Bed Thermocline Tank (MLPBTT).

The geometry parameters of the SLPBTT are the same as those of the MLPBTT. Each tank consists of a packed-bed region, a tank wall, two insulation layers and two distributors. The diameter (D) of the packed-bed region is 3.0 m and its height (H) is 5.9 m. The thermal energy storage region contains the solid filler and molten salt. The void fraction (ε) of salt in the packed-bed region is 0.22. The filler is assumed to be a sphere and it is uniformly distributed in the packed-bed region, and the average diameter of the sphere (d_p) is 19.05 mm. The tank wall with the thickness (l_{st}) of 0.04 m is made of stainless steel. Two insulation layers with the thickness (l_{in}) of 0.2 m are coated inside and outside the stainless steel wall, respectively. The heat transfer fluid (HTF) is Solar Salt (60wt% $NaNO_3$, 40wt% KNO_3). The thermal physical properties of tank body and that of molten salt are shown in Table 1 [42]. The properties of five alternative fillers, including high-temperature concrete, Silicon Carbide, Alumina Ceramics, cast iron, and quartzite rock are listed in Table 2 [32].

Table 1. The properties of tank body materials and molten salt [42].

Materials	ρ_s/(kg·m^{-3})	$c_{p,s}$/(J·kg^{-1}·K^{-1})	k_s/(W·m^{-1}·K^{-1})	μ/(kg·m^{-1}·s^{-1})
Insulation layer	2000	960	0.1	-
Steel wall	7800	470	35.0	-
Molten salt	2090-0.636T(°C)	1443+0.172T(°C)	0.113+1.9×10^{-4}T(°C)	[22.714-0.12T(°C)+2.281×10^{-4}T(°C)^2-1.474×10^{-7}T(°C)^3] ×10^{-3}

Table 2. The properties of 5 solid fillers [32].

Materials	ρ_s/(kg·m^{-3})	$c_{p,s}$/(J·kg^{-1}·K^{-1})	k_s/(W·m^{-1}·K^{-1})	$\rho_s c_{p,s}$/(MJ·m^{-3}·K^{-1})
High-temp. concrete	2750	916	1.0	2.519
Silicon Carbide	3210	750	120	2.408
Alumina Ceramics	3750	780	30	2.925
cast iron	7900	837	29.3	6.612
quartzite rock	2500	830	5.6	2.075

In the operation, the operational principles of tanks are presented as follows. During the charging process, the high-temperature salt ($T_{C,in}$=390°C) flows into the packed-bed region after though the distributor. The cold filler is heated, and the cooled salt flows out from the bottom of the tank. The outlet salt temperature ($T_{C,out}$) will be increased from 290°C while the thermocline region arrives at the bottom of the tank. The charging process will be stopped when the value of $T_{C,out}$ has been increased to the threshold value ($T_{C,th}$). On the contrary, during the discharging process, the low-temperature salt ($T_{D,in}$=290°C) from the bottom of the tank will be heated by the hot filler. The heated salt flows out of the top of the tank. The outlet salt temperature ($T_{D,out}$) starts will be decreased from 390°C while the thermocline region arrives at the top of the tank. The discharging process will be stopped when the value of $T_{D,out}$ has been reduced to the threshold value ($T_{D,th}$). In the study, under the restriction of steam generation and solar field, the value of threshold temperature was determined by Eq. (1) [36].

$$\begin{aligned} \theta_C &= \left(T_{C,th} - T_{D,in}\right)/\left(T_{C,in} - T_{D,in}\right) = 0.39; \quad \text{Charging} \\ \theta_D &= \left(T_{D,th} - T_{D,in}\right)/\left(T_{C,in} - T_{D,in}\right) = 0.74; \quad \text{Discharging} \end{aligned} \tag{1}$$

where $T_{C,th}$ and $T_{D,th}$ are 329°C and 364°C, respectively.

2.2 Mathematical model

In this section, a transient, two-dimensional, axisymmetric, and local thermal non-equilibrium model is developed to analyze the effect of thermocline thickness on the thermal performance of the PBTT. First, the governing equations for the model and the boundary conditions of the computation region are expressed in Section 2.2.1 and Section 2.2.2, respectively. Then, the initial condition and solution methods of the model are introduced in Section 2.2.3. Finally, several parameters are defined to analyze the thermal characteristics of the PBTT in Section 2.2.4. The scheme of the computational domain is shown in Fig. 3. In the study, the assumptions are presented primarily to simplify the mathematical model as follows.

(1) The thermal properties of filler are constant. The filler is placed uniformly in the packed-bed region that can be regarded as a homogeneous, continuous, and isotropic porous medium.

(2) The salt flow is uniform and symmetrical about the axis under the effect of a distributor at the inlet of the packed-bed region. In the packed-bed region, the salt flow can be treated as laminar and incompressible flow.

(3) The salt temperature is uniform at the inlet of a tank. There is no temperature undulation during a charging process and discharging process.

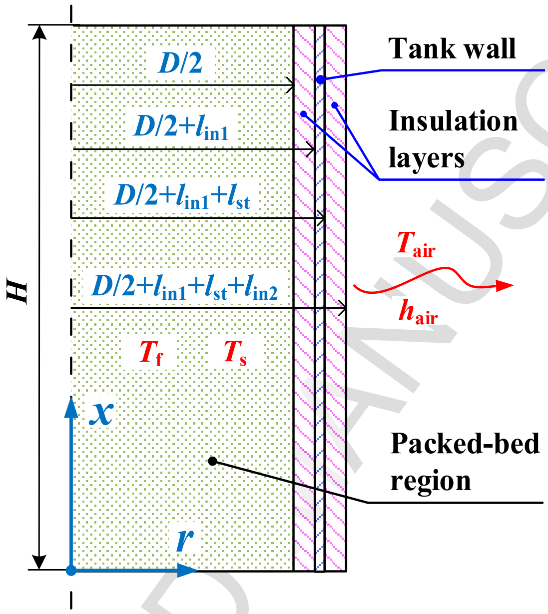

Fig. 3. Sketch of the computational domain.

2.2.1 Governing equations

The governing equations for the model are expressed in Eq. (2)-(6) [43, 44], and the details are as follows.

Continuity equation for molten salt:

$$\varepsilon \frac{\partial \rho_{\mathrm{f}}}{\partial t} + \nabla \cdot [\rho_{\mathrm{f}} \vec{u}] = 0 \tag{2}$$

where ε is the porosity of the packed-bed region, ρ_{f} is the density of molten salt, and $\vec{u}$ is the superficial velocity vector based on the cross-sectional area of fluid (salt) and porous medium (filler).

Momentum equation for molten salt:

$$\frac{\partial\left(\rho_{\mathrm{f}}\vec{u}\right)}{\partial t}+\nabla\cdot\left(\rho_{\mathrm{f}}\vec{u}\vec{u}\right)=\nabla\cdot(\mu\nabla\vec{u})-\nabla p+\rho_{\mathrm{f}}\vec{g}-\frac{\mu}{K}\vec{u}-C_2\cdot\frac{1}{2}\rho_{\mathrm{f}}\left|\vec{u}\right|\vec{u} \tag{3}$$

where μ is the viscosity of salt, K is the permeability of the packed-bed region evaluated as $K=d_{\mathrm{p}}^{2}\varepsilon^{3}/[150(1-\varepsilon)^{2}]$, and C_2 is the inertial coefficient evaluated as $C_2=3.5/\sqrt{150K\varepsilon^{3}}$.

Energy equation for molten salt:

$$\varepsilon\frac{\partial(\rho c_p)_{\mathrm{f}}T_{\mathrm{f}}}{\partial t}+\nabla\cdot[(\rho c_p)_{\mathrm{f}}T_{\mathrm{f}}\vec{u}]=\nabla\cdot(k_{\mathrm{f,eff}}\nabla T_{\mathrm{f}})+h_V(T_{\mathrm{s}}-T_{\mathrm{f}}) \tag{4}$$

Energy equation for solid filler:

$$(1-\varepsilon)(\rho c_p)_{\mathrm{s}}\frac{\partial T_{\mathrm{s}}}{\partial t}=\nabla\cdot(k_{\mathrm{s,eff}}\nabla T_{\mathrm{s}})-h_V(T_{\mathrm{s}}-T_{\mathrm{f}}) \tag{5}$$

Energy equation for the tank wall and insulation layers:

$$\frac{\partial(\rho_i c_{p,i}T_i)}{\partial t}=\nabla\cdot(k_i\nabla T_i) \tag{6}$$

where c_{p}, T, k, and h_V represent heat capacity, temperature, effective thermal conductivity, and the volumetric interstitial heat transfer coefficient between the salt and filler, respectively. The subscript f, s, i, and eff represent salt, filler, insulation layers, and effective, respectively.

The volumetric interstitial heat transfer coefficient (h_V) can be calculated by Eq. (7) [45].

$$h_V=\frac{6(1-\varepsilon)k_{\mathrm{f}}[2+1.1Re_{\mathrm{p}}^{0.6}Pr^{1/3}]}{d_{\mathrm{p}}^{2}} \tag{7}$$

The effective thermal conductivity of salt and filler ($k_{\mathrm{f,eff}}$, $k_{\mathrm{s,eff}}$) can be calculated by Eq. (8) [46].

$$k_{\text{f,eff}} = \begin{cases} 0.7\varepsilon k_{\text{f}}, & Re_{\text{p}} \le 0.8 \\ 0.5 Pr Re_{\text{p}} k_{\text{f}}, & Re_{\text{p}} > 0.8 \end{cases}$$
$$k_{\text{s,eff}} = k_{\text{all,eff}} - k_{\text{f,eff}} \tag{8}$$
$$k_{\text{all,eff}} = k_{\text{f}} (k_{\text{s}} / k_{\text{f}})^{m} + 0.5 k_{\text{f}} Pr Re_{\text{p}}$$
$$m = 0.28 - 0.757 \ln \varepsilon - 0.057 \ln(k_{\text{s}} / k_{\text{f}})$$

2.2.2 Boundary conditions

The boundary conditions of the computation region are introduced in this section. For the bottom of the packed-bed region (i.e., x=0, 0≤r≤D/2), the cold salt enters through the boundary during a discharging process. The inlet condition of constant velocity (u_{in}=4.186×10^{-4} m·s^{-1}) and constant temperature of salt ($T_{\text{D,in}}$) are determined by Eq. (9). During a charging process, the cooled salt flows out of this boundary, and the fully developed condition is employed in Eq. (10) .

$$\text{Discharging:}\; u = u_{\text{in}}, v = 0,\;\; T_{\text{f}} = T_{\text{D,in}},\; k_{\text{f,eff}} \frac{\partial T_{\text{s}}}{\partial x} = 0 \tag{9}$$

$$\text{Charging:}\; \frac{\partial u}{\partial x} = 0,\;\; v = 0,\;\; \frac{\partial T_{\text{f}}}{\partial x} = 0,\;\; k_{\text{f,eff}} \frac{\partial T_{\text{s}}}{\partial x} = 0 \tag{10}$$

For the top of the packed-bed region (i.e., x=H, 0≤r≤D/2), the heated salt flows out of this boundary during a discharging process, and the fully developed condition in Eq. (11) is employed. During a charging process, the hot salt enters through this boundary, and the inlet condition of u_{in} and $T_{\text{C,in}}$ are determined by Eq. (12).

$$\text{Discharging:}\; \frac{\partial u}{\partial x} = 0,\;\; v = 0,\;\; \frac{\partial T_{\text{f}}}{\partial x} = 0,\;\; k_{\text{f,eff}} \frac{\partial T_{\text{s}}}{\partial x} = 0 \tag{11}$$

$$\text{Charging:}\; u = u_{\text{in}},\;\; v = 0,\;\; T_{\text{f}} = T_{\text{C,in}},\;\; k_{\text{f,eff}} \frac{\partial T_{\text{s}}}{\partial x} = 0 \tag{12}$$

For the symmetry axis of the cylindrical tank (i.e., 0≤x≤H, r =0), the symmetrical boundary conditions of the salt temperature (T_{f}) and filler temperature (T_{s}) are employed in Eq. (13).

$$\frac{\partial u}{\partial r} = 0,\;\; v\text{=}0,\;\; \frac{\partial T_{\text{f}}}{\partial r} = \frac{\partial T_{\text{s}}}{\partial r} = 0 \tag{13}$$

For the surface of the tank (i.e., 0≤x≤H, r =D/2+l_{in1}+l_{st}+l_{in2}), the heat is transferred from this boundary into the ambient air through forced convection. The boundary condition is determined by Eq. (14).

$$-k_{\mathrm{in2}}\frac{\partial T_{\mathrm{in2}}}{\partial r}=h_{\mathrm{air}}\left(T_{\mathrm{in2}}-T_{\mathrm{air}}\right) \quad (14)$$

where h_{air} is the convective heat transfer coefficient between ambient air and the insulation layer, and T_{air} is the temperature of ambient air.

For the inner surface of the insulation layer connecting filler and salt (i.e., $0\le x\le H$, $r=D/2$), the non-slip boundary condition is employed. Moreover, the heat exchanges of the interface between salt and insulation layer, and the heat transfer between filler and insulation layer is zero because of the contactless surface area and negligible radiation. The conditions of the inner surface are determined by Eq. (15).

$$u=v=0,\quad T_{\mathrm{f}}=T_{\mathrm{in1}},\quad k_{\mathrm{f,eff}}\frac{\partial T_{\mathrm{f}}}{\partial r}=k_{\mathrm{in1}}\frac{\partial T_{\mathrm{in1}}}{\partial r},\quad k_{\mathrm{s,eff}}\frac{\partial T_{\mathrm{s}}}{\partial r}=0 \quad (15)$$

There is no heat transfer at the boundary of the cross section of the stainless steel tank wall.The insulation layers at the bottom and top of the packed-bed region (i.e., $x=0$ & $x=H$, $D/2\le r\le D/2+l_{\mathrm{in1}}+l_{\mathrm{st}}+l_{\mathrm{in2}}$), and the adiabatic condition in Eq. (16) is employed.

$$\frac{\partial T_{\mathrm{in1}}}{\partial x}=\frac{\partial T_{\mathrm{st}}}{\partial x}=\frac{\partial T_{\mathrm{in2}}}{\partial x}=0 \quad (16)$$

2.2.3 Initial conditions and solution methods

The tank is filled with salt at the beginning of the cyclic processes. Both of T_{f} and T_{s} all over the tank are equal to $T_{\mathrm{C,in}}$ (390°C). The forced convection heat transfer between the tank and air is steady with T_{air}=30°C and h_{air}=10 W·m^{-2}·K^{-1}. The fluid is motionless in the tank before the start of the cyclic processes.

The governing equations were numerically solved using the finite volume method in the Ansys Fluent 14.0 software [44]. The programmed user-defined functions (UDFs), including the fluid energy source, the solid energy source and the unsteady solid energy term, are coupled with Ansys Fluent 14.0 solver to compute the model equations. The pressure-velocity coupling field is solved by the SIMPLE algorithm. The momentum equations and energy equations are both discretized by the second-order upwind scheme. A time step of 5s and the max iterations of 50 for each step are employed during calculating.

2.2.4 Parameter definitions

Several parameters are defined as follows to analyze the thermal characteristics of the PBTT.

The ideal stored thermal energy of tank (Q_{ideal}) is defined as the maximum thermal energy stored in a tank within the operational molten salt temperature ranging from $T_{\mathrm{D,in}}$ to $T_{\mathrm{C,in}}$, which is calculated by Eq. (17).

$$Q_{\mathrm{ideal}}=\left(T_{\mathrm{C,in}}-T_{\mathrm{D,in}}\right)\cdot H\frac{\pi D^2}{4}\cdot\left(\varepsilon\rho_{\mathrm{f}}c_{p,\mathrm{f}}+\left(1-\varepsilon\right)\sum_{j}^{n}h_j\rho_{\mathrm{s},j}c_{p,\mathrm{s},j}\right) \tag{17}$$

where the subscripts j indicates different kind of solid filler materials, and h_j represents the ratio between filling height of one filler (H_j) to packed-bed region height (H), evaluated as $h_j=H_j/H$.

The effective charging time (t_{C}) is the time when $T_{\mathrm{C,out}}$ is lower than $T_{\mathrm{C,th}}$. Similarly, the effective discharging time (t_{D}) is the time when $T_{\mathrm{D,out}}$ is higher than $T_{\mathrm{D,th}}$. The stored thermal energy in charging process (Q_{C}) is defined as the thermal energy stored in the tank during t_{C}. Similarly, the released thermal energy in discharging process (Q_{D}) is defined as the thermal energy transferred from the tank to salt during t_{D}. Q_{C} and Q_{D} are determined by Eq. (18).

$$\begin{aligned}Q_{\mathrm{C}}&=u_{\mathrm{in}}\frac{\pi D^2}{4}\cdot\int_0^{t\le t_{\mathrm{C}}}\rho_{\mathrm{f}}c_{p,\mathrm{f}}\left(T_{\mathrm{C,in}}-T_{\mathrm{C,out}}\left(t\right)\right)dt\\Q_{\mathrm{D}}&=u_{\mathrm{in}}\frac{\pi D^2}{4}\cdot\int_0^{t\le t_{\mathrm{D}}}\rho_{\mathrm{f}}c_{p,\mathrm{f}}\left(T_{\mathrm{D,out}}\left(t\right)-T_{\mathrm{D,in}}\right)dt\end{aligned} \tag{18}$$

The charging efficiency (η_C) or discharging efficiency (η_D) is defined as the ratio of Q_C (or Q_D) to the Q_{ideal} of the tank, which is determined by Eq. (19).

$$\eta_C = Q_C / Q_{ideal}; \quad \eta_D = Q_D / Q_{ideal} \tag{19}$$

The periodic state is defined as the variation of the stored energy and the released energy from cycle i to cycle (i-1) is less than 1.0 % as shown in Eq. (20).

$$\left| \frac{Q_{C,i} - Q_{C,i-1}}{Q_{C,i}} \right| \le 1.0\% \ , \quad \left| \frac{Q_{D,i} - Q_{D,i-1}}{Q_{D,i}} \right| \le 1.0\% \tag{20}$$

where the subscript i represents the number of ith cycle.

The thermocline thickness (L) is the covering length of the thermocline region, which is determined by Eq. (21).

$$L = \begin{cases} x(T_h) - 0 \ , & T_{s,in} > T_l \\ x(T_h) - x(T_l), & T_{s,in} \le T_l \text{ and } T_{s,out} \ge T_h \\ H - x(T_l), & T_{s,out} < T_h \end{cases} \tag{21}$$

where T_h and T_l are the critical high and low temperature of thermocline region, respectively. In this study, T_h and T_l are chosen to be 385°C ($T_{C,in}$-5°C) and 295°C ($T_{D,in}$+5°C) , respectively. $T_{s,in}$ and $T_{s,out}$ represent the temperatures of filler at the inlet and outlet, respectively.

2.3 Cost model for the thermocline TES system

The direct costs including the filler cost, container cost, and the cost of purchased equipment are considered as the total capital cost of a thermocline TES system ($C_{TES,total}$) [22]. The filler cost is evaluated by weight as shown in Table 3 [47, 48].The container costs include the costs of carbon steel, insulation, foundation and platform as shown in Table 3 [47, 48]. The carbon steel and insulation costs are evaluated by the cover area of the tank, and the foundation and platform costs are evaluated by foundation area of the tank. The cost of the purchased equipment is shown in Table 4 when Q_D=100 MWht [22]. The capital cost per kWht of the system (C_{TES}) is defined as the ratio of the total capital cost ($C_{TES,total}$) to the released thermal energy (Q_D), which is determined by Eq.

(22).

$$C_{\mathrm{TES}} = C_{\mathrm{TES,total}} / Q_{\mathrm{D}} \quad (22)$$

Table 3 Cost details of filler and container for thermocline storage tank [47, 48].

Filler	Unit cost	Container	Unit cost
Quartzite rock, \$ ton^{-1}	13	Carbon steel of cover, \$ m^{-2}	3799
Cast iron, \$ ton^{-1}	465	Insulation of cover , \$ m^{-2}	206
Concrete, \$ ton^{-1}	105	Foundation of tank, \$ m^{-2}	1199
		Platform of tank, \$ m^{-2}	292

Table 4 Cost details of purchased equipment for thermocline storage tank [22].

Purchased equipment	Cost for Q_D=100 MWht	Purchased equipment	Cost for Q_D=100 MWht
Salt melting system, k\$	1420	Distributors, k\$	100
Electrical, k\$	179	Surge tanks, k\$	32
Preheating equipment, k\$	215	Pumps & PCE, k\$	1170
Interconnecting piping & valves, k\$	464	Instrumentation & controls, k\$	293

3. Grid independence test and model validation

3.1 Grid independence test

A grid independence test is conducted to guarantee the accuracy of the computation, and the variations of molten salt temperature (T_f) at different positions for seven grid systems and different discharging times (x=2.5 m, r=0 m, t=56 min; x=5.0 m, r=0 m, t=146 min) are shown in Fig. 4. The seven grid systems (Axial grid number × Radial grid number) are 60×35, 80×45, 100×55, 110×65, 120×75, 140×90, 160×110, respectively. It can be found out that there is a wide variation of T_f when the grid number is below 7150 (110×65) in Fig. 4. However, the T_f almost remains the same when the grid number is larger than 7150. So, the fifth grid model (120×75) is used in the following simulations after considering the computational accuracy and time.

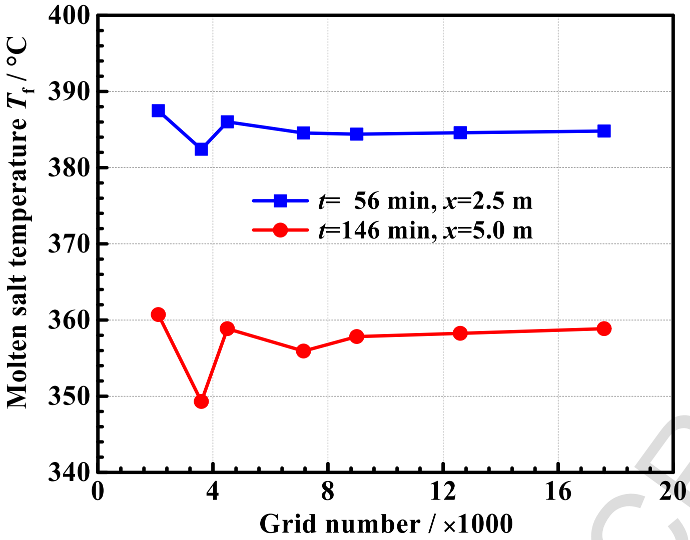

Fig. 4. Grid independence test.

3.2 Model validation

The model is validated by comparing the axial variation of T_f at the different discharging time obtained from the present numerical results with the experimental results reported by Pacheco et al.[23]. It can be observed in Fig. 5 that the present temperature profiles are similar to the experimental results. However, the experimental results indicate some scatter due to the uncontrolled environmental condition. Generally, considering the uncertainty in experimental test and the assumptions in numerical calculation, the agreement between the present numerical results and experimental results is satisfactory. The good agreement indicates that the numerical model is accurate and reliable.

ACCEPTED MANUSCRIPT

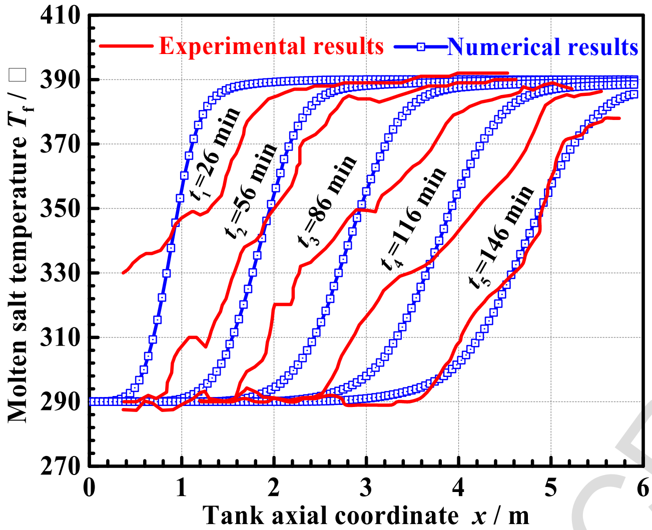

Fig. 5. Comparison between present numerical result of the axial molten salt temperature and the experimental results from Pacheco et al.[23].

4. Results and discussions

The thermal performance of thermal storage subsystem is one of the major factors to determine the electricity-generation power and efficiency of the CSP. The thermal storage subsystem keeps repeating charging and discharging processes in the operation, so cyclic thermal performance of this subsystem is of primary interest and is studied in following sections.

4.1 Thermal performance of the SLPBTT in cyclic processes

In this section, the thermal performance of a SLPBTT in cyclic processes is analyzed. The variations of key performance parameters are analyzed, and the temperature distributions are revealed in the periodic state. Moreover, the effects of the thermocline on the thermal performance are discussed.

4.1.1 Variations of useful energy and efficiency

Fig. 6 shows the variations of Q_C, Q_D, η_C, and η_D in cyclic processes for a SLPBTT. It can be observed that Q_C, Q_D, η_C, and η_D decrease with increasing cycle numbers. Specifically, it can be found that all the four parameters decrease sharply from Cycle 1 to Cycle 2, while the variations are small among Cycle 2 to Cycle 4. This is because the tank is fully charged for Cycle 1 with $Q_{C,1}=Q_{ideal}$ and $\eta_{C,1}$=100%. However, in subsequent cycles, the tank could not be fully charged or discharged due to the limitation of outlet temperature. It also can be proved that the variations of parameters between Cycle 3 and Cycle 4 are lower than 0.7%, which means the charging and discharging processes enter a periodic state from Cycle 3. In addition, Q_D is lower than Q_C at the periodic state, and around 2.7% of Q_D is lost because of the convective heat transfer between the tank wall and air.

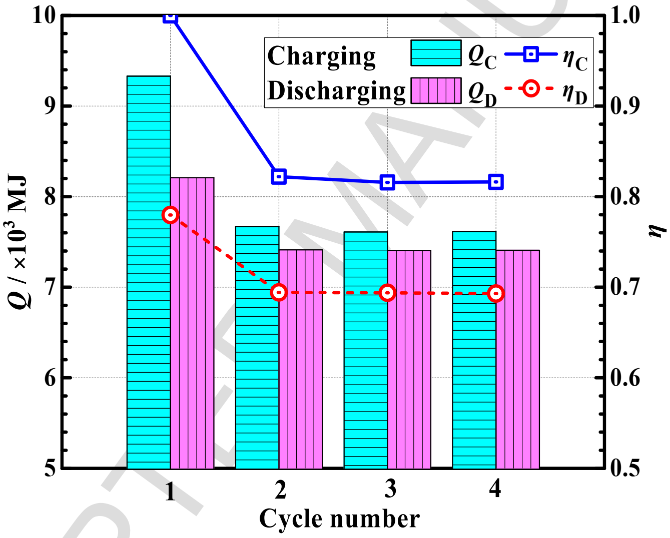

Fig. 6 Variation on Q_C, Q_D, η_C and η_D with cycles.

4.1.2 Temperature distribution and thermocline expansion

Fig. 7 demonstrates the axial temperature distributions of molten salt at different times (t_1=0 h, t_2=1.2 h, t_3=t_D or t_C) of the charging and discharging processes in the periodic state. It can be seen from Fig. 7 that there is a large-temperature-gradient region called thermocline, segregating the hot region (T=390°C) and cold region (T=290°C) in the tank. The thermocline region moves downward during the charging process and upward during the discharging process. It is also can be seen in Fig. 7 that there is a retention thermocline region at the end of charging or discharging process (t_3) due to the limitation of outlet salt temperature.The thickness of retention thermocline of charging process (1.5 m) is smaller than that of discharging process (1.8 m).

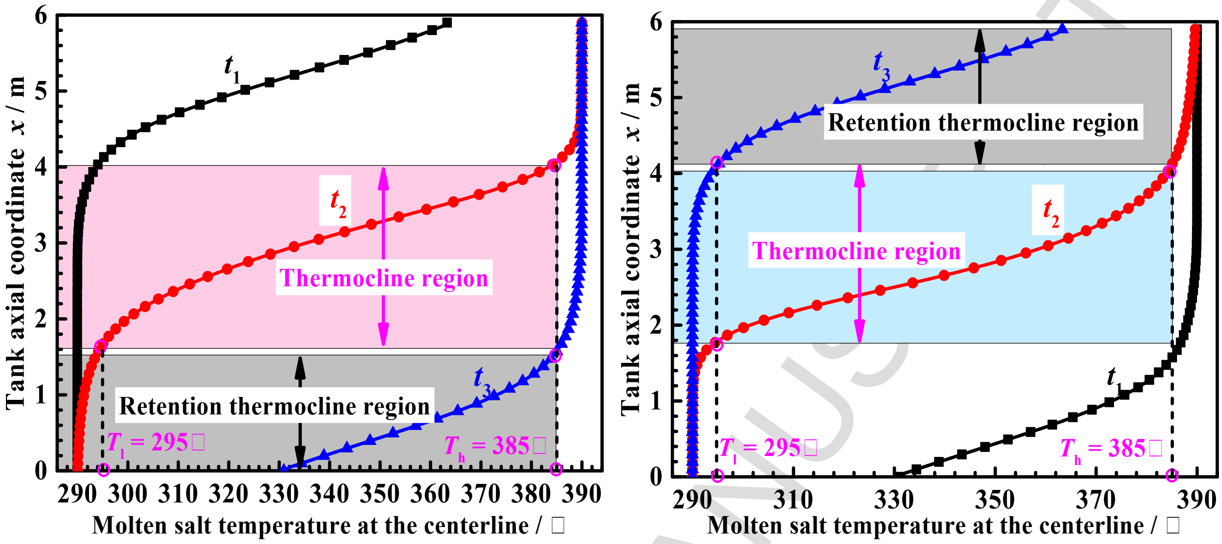

(a) Charging (b) Discharging

Fig. 7 Axial temperature distributions of salt at t_1=0 h, t_2=1.2 h and t_3=t_D or t_C in the periodic state.

Fig. 8 shows the variation of the thermocline thickness (L) with cycles. The L varies greatly in each charging or discharging process, and it expands firstly from the beginning of a process, and then reaches a peak when the thermocline arrives at the outlet.Finally it drops sharply until the end of process. It is also observed that the retention thermocline expands slightly with cycles before the cycle enter a periodic state after Cycle 3, e.g., L_R for the discharging process increases from 1.67 m in Cycle 1 to 1.77 m in Cycle 3.

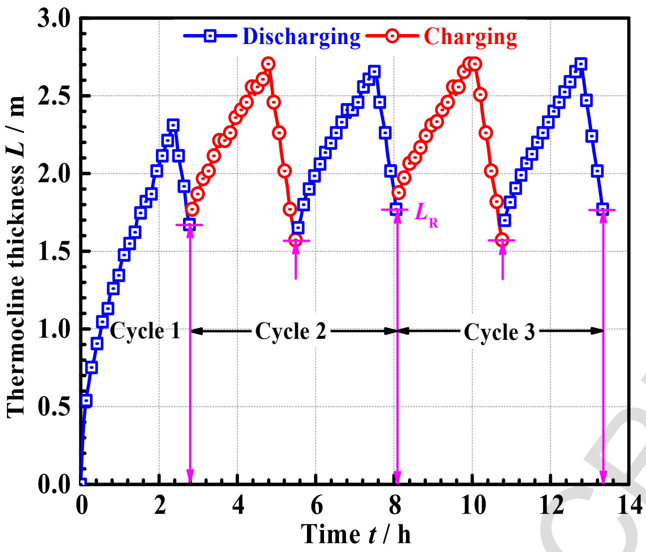

Fig. 8 Variation of thermocline thickness L with cycles.

4.1.3 Effect of thermocline on thermal performance

The axial temperature distributions of salt at the final state of charging and discharging processes in a periodic cycle are given in Fig. 9. At the end of the charging process, there is a retention thermocline region at the bottom of the tank, so this part is not fully charged. As a result, the stored energy (Q_C) is smaller than the ideal stored energy (Q_{ideal}) of SLPBTT. Region 1 in Fig. 9 indicates the energy storage ability wasted (Q_1) due to the partially charging.

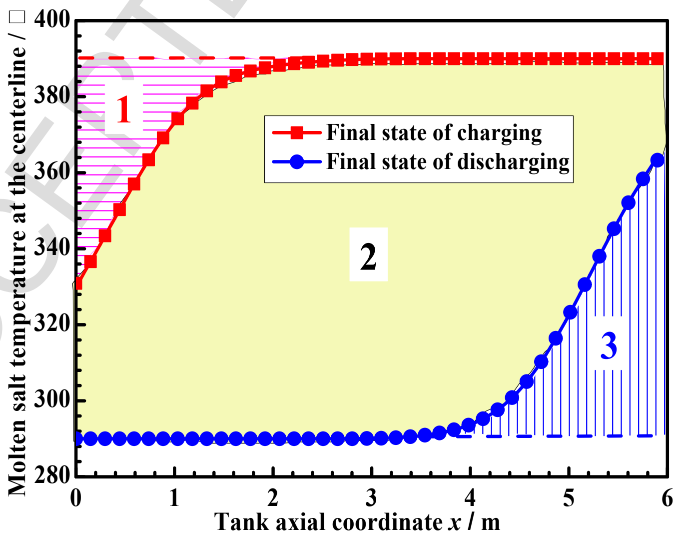

Fig. 9 Axial temperatures of salt at final state of charging and discharging processes at periodic cycle.

Similarly, at the end of discharging process, there is a retention thermocline region at the top of the tank, so this part is not fully discharged. It means that the released energy (Q_D) is smaller than Q_{ideal}. Region 3 in Fig. 9 indicates the energy discharging ability wasted (Q_3) because of the partially discharging. The region 2 of Fig. 9 indicates the sum (Q_2) of the stored energy (Q_C) and the heat loss ($Q_{C,loss}$) in the charging process, or it presents the released energy (Q_D) and the heat loss ($Q_{D,loss}$) in the discharging process. The relationships of these parameters are expressed in Eq. (23) and (24).

$$\begin{aligned} Q_{ideal} &= Q_1 + Q_2 + Q_3 \\ Q_2 &= Q_C + Q_{C,loss} = Q_D + Q_{D,loss} \end{aligned} \tag{23}$$

$$\begin{aligned} \eta_C &= Q_C / Q_{ideal} = \left(Q_2 - Q_{C,loss}\right) / Q_{ideal} \\ \eta_D &= Q_D / Q_{ideal} = \left(Q_2 - Q_{D,loss}\right) / Q_{ideal} \end{aligned} \tag{24}$$

The efficiency of the SLPBTT (η) is the ratio of the useful energy (Q_C, Q_D) to the ideal stored energy (Q_{ideal}). Q_{ideal} will remain unchanged if the structure of SLPBTT is defined. Hence, for improving η, the numerators (Q_2-$Q_{C,loss}$, Q_2-$Q_{D,loss}$) in Eq. (24) should be increased by reducing $Q_{C,loss}$ and $Q_{D,loss}$, and increasing Q_2. On the one hand, $Q_{C,loss}$ and $Q_{D,loss}$ can be reduced by enhancing the insulation of the wall. On the other hand, Q_2 can be increased by reducing Q_1 and Q_3. It can be provided that if the retention thermocline becomes thinner, lower Q_1 and Q_3 will be achieved in Fig. 9 . For reducing the retention thermocline thickness, the proper approach is to control the expansion of thermocline.

From the above analysis, it has been found that the thermal performance of SLPBTT varies with cycles, thresholds of outlet temperatures and time. The retention thermocline of the previous cycle has direct effects on thermal performance.

4.2 The interface effect on thermocline

In this section, first, the effects of five promising solid fillers on the thermocline expansion in the SLPBTT are investigated. Then, a phenomenon is first reported and analyzed which is called interface effect between two different fillers on thermocline development..

4.2.1 Effect of fillers on thermocline expansion

The effect of different fillers on the thermocline expansion is discussed by comparing the thermocline thickness (L) in discharging for Cycle 1.The influences of five promising fillers given in Table 2 as shown in Fig. 10. It is seen that the expanding velocity of L and the retention thermocline thickness (L_R) vary with solid fillers.

For the fillers with similar volumetric heat capacity ($\rho_s c_{p,s}$) of 2.075~2.925 MJ·m^{-3}·K^{-1} as given in Table 2, Silicon Carbide owns the thickest L_R and the fastest expanding velocity of L, followed by Alumina Ceramics, quartzite rock, and high-temperature concrete. This is because the filler with larger thermal conductivity (k_s) will result in more significant thermal diffusion, which leads to larger L_R and faster expanding velocity of L, and vice versa.

For the cast iron with the volumetric heat capacity ($\rho_s c_{p,s}$) of 6.612 MJ·m^{-3}·K^{-1} which is much larger than those of other fillers, the expanding velocity of L is the second lowest one among the five. However, L_R is relatively large and claims the second largest position, even its conductivity (k_s=29.3W·m^{-1}·K^{-1}) is not very large. This is because the expansion time for thermocline in cast iron is quite long, which results in the large L_R at a relatively low expanding velocity.

As mentioned before, η_C and η_D increase with the decreasing retention thermocline thickness. Therefore quartzite rock and high-temperature concrete with small L_R are recommended as solid filler based on the above analysis. In addition, for increasing the useful energy (Q_C, Q_D), the cast iron with large $\rho_s c_{p,s}$ is suggested.

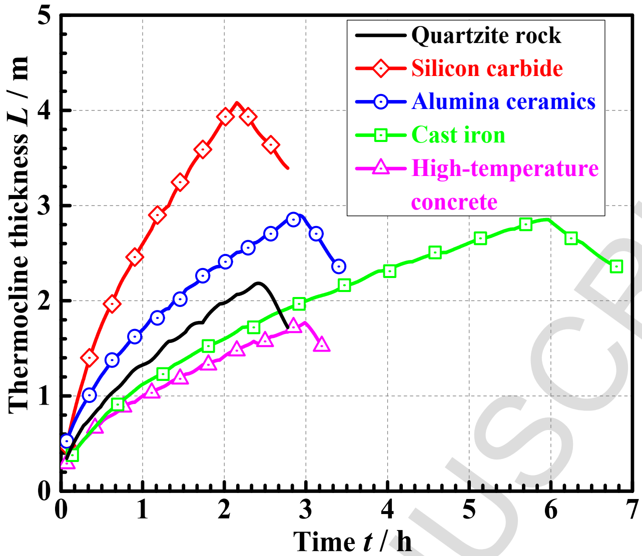

Fig. 10 Variations of thermocline thickness with discharging time for 5 solid fillers in Cycle 1.

4.2.2 The interface effect on thermocline development

From previous analysis, it is found that the thermocline expanding velocity varies with the change of filler materials. If a tank is filled with two different fillers orderly, which constitute the Multi-Layered Packed-Bed Thermocline Tank (MLPBTT) with two layers, there will be an interface between the two layers. The effect of the interface on thermocline development, which can be divided into the expanding effect and shortening effect, will be observed. The interface effect in discharging is taken as an example to illustrate the phenomenon, where the thicknesses of lower and upper layers are 2.5 m and 3.4 m, and the cast iron and quartzite rock are adopted as fillers. Fig. 11 and Fig. 12 show the expanding effect and shortening effect on thermocline development, respectively.

In the expanding effect case, cast iron is placed at the bottom of the tank, and quartzite rock is placed at the top. When thermocline flows from cast iron to quartzite rock, the thickness of the thermocline (L) in Fig. 11(b) during the crossing process becomes much thicker than that before crossing the interface in Fig. 11(a). This is because the expanding velocity of the thermocline in the quartzite rock is quicker as shown in Fig. 10. The phenomenon, which is the thermocline thickness increases sharply when the thermocline crosses the filler interface, is defined as the "expanding effect".

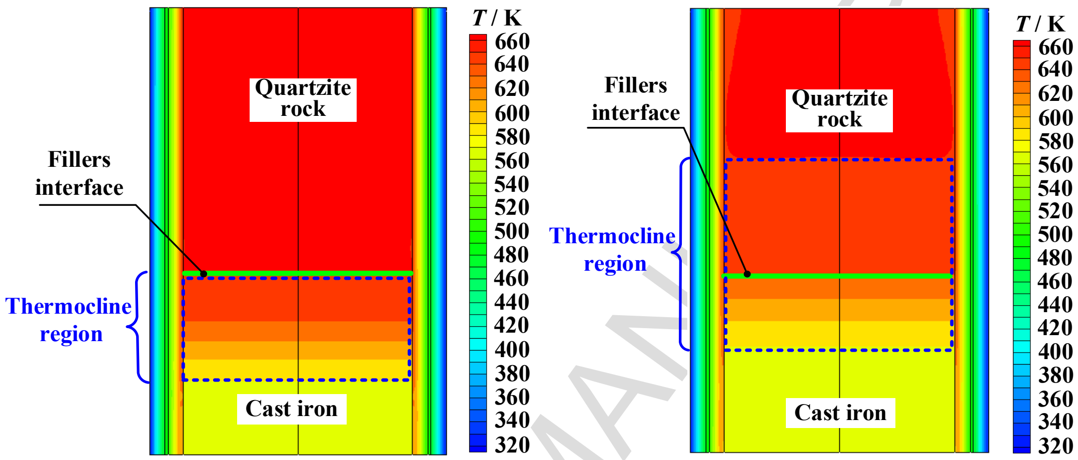

(a) Before crossing the interface. (b) During the crossing process.

Fig. 11. Expanding effect on salt temperature distribution in discharging.

Furthermore, in the shortening effect case, quartzite rock is placed at the bottom of the tank, and cast iron is placed at the top. When thermocline flows from quartzite rock to cast iron, it can be seen that L in Fig. 12(b) during the crossing process becomes thinner than that before crossing the interface in Fig. 12(a). This phenomenon, which is the thermocline thickness decreases when the thermocline crosses the interface, is defined as the "shortening effect".

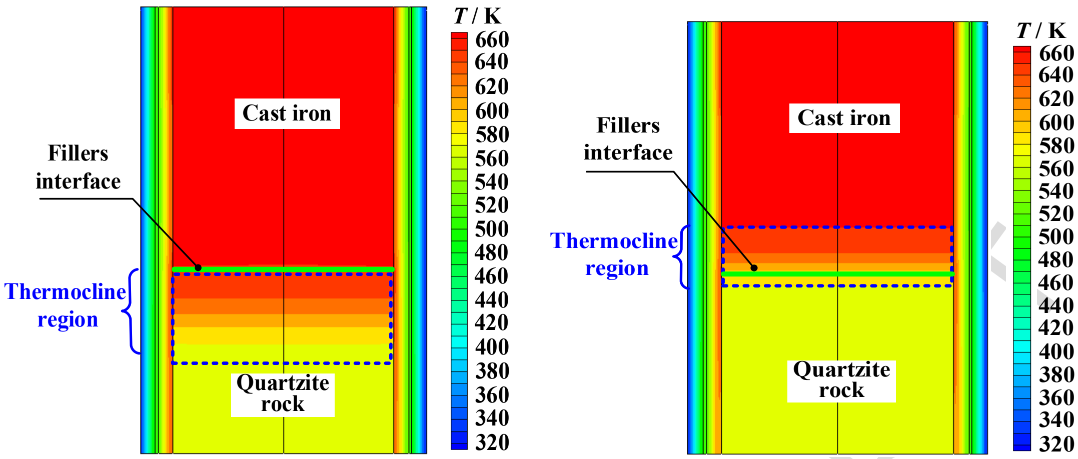

(a) Before crossing the interface. (b) During the crossing process.

Fig. 12. Shortening effect on salt temperature distribution in discharging.

Through the above discussion, an interesting issue has been proposed that the development of thermocline can be controlled by utilizing the interface effect in a reasonable way to improve the thermal performance.

4.3 Thermal performance of the MLPBTT in cyclic processes

In this part, a novel multi-layered design using several different fillers is primarily proposed. After that, the effects of layer structures are discussed, and some suggestions are provided.

4.3.1 The design of a novel MLPBTT

A novel MLPBTT shown in Fig. 2 is designed in the following way to optimize the thermal performance, including the useful energy and thermal efficiencies.

First, to improve the charging and discharging efficiencies (η_C, η_D), the cheap quartzite rock with small L_R are chosen as the primary solid filler based on the results in Section 4.2.1.A thickness of 3.5m is designed to achieve a relatively low cost after considering the price. To increase the useful energy (Q_C, Q_D), a relatively thin layer of cast iron with large $\rho_s c_{p,s}$ is also chosen. In addition, to control the expansion of thermocline, high-temperature concrete with the lowest conductivity (k_s) is used.

Second, if cast iron is placed at the top of the tank, a large proportion of the stored energy will be left in tank and wasted in discharging. However, if cast iron is placed at the bottom of the tank, its storage ability will not be adequately unitized in charging. For these reasons, the cast iron should be placed in the middle of the tank, and other two fillers are placed near the upper and lower borders, respectively.

Finally, the following items are optimized for controlling the development of the thermocline thickness to improve the thermal performance including positions of quartzite rock and high-temperature concrete, and the thicknesses of the high-temperature concrete and cast iron..

Fourteen layer structures are designed by using the above procedures. The considering positions and ratios of the fillers are shown in Table 5. These structures can be divided into group A and group B. In group A including structures A-1 to A-7, the quartzite rock is placed at the bottom, and high-temperature concrete is placed at the top. In group B including structures B-1 to B-7, the high-temperature concrete is placed at the bottom and quartzite rock is placed at the top. The thicknesses of the layers in structure A-*i* is the same as that in corresponding structure B- *i* as given in Table 5. Moreover, the typical SLPBTTs using quartzite rock, cast iron and high-temperature concrete are also listed in Table 5.

After conducting the examination in the similar way as shown in section 4.1.1, it is also found that the charging and discharging processes of all structures will enter a periodic state from Cycle 3. Therefore, Cycle 3 is chosen as the periodic state in the subsequent study.

Table 5. Structures of fourteen MLPBTTs and three SLPBTTs.

Structures	Percentages of the fillers' height /m		
	High-temp. concrete	Cast iron	Quartzite rock
S-quartzite	0	0	100%
S-iron	0	100%	0
S-concrete	100%	0	0
A-1/B-1	40.68%	0	59.32%
A-2/B-2	35.59%	5.08%	59.32%
A-3/B-3	30.51%	10.17%	59.32%
A-4/B-4	20.34%	20.34%	59.32%
A-5/B-5	10.17%	30.51%	59.32%
A-6/B-6	5.08%	35.59%	59.32%
A-7/B-7	0	40.68%	59.32%

4.3.2 Variation of thermal performance and cost analysis

It has been demonstrated that the thermal performance (Q_C, Q_D, η_C, η_D) of the 14 structures in two groups in a period cycle in Fig. 13. The results show that the variations of η_C and η_D between structure A-1 in group A and corresponding structure B-1 in group B are around 2.0%.In respect of other structures, the variations are within 1.0%. This result indicates that the effects of positions of quartzite rock and high-temperature concrete in the MLPBTT on thermal performance can be negligible. Therefore, group A will be taken as the example for further discussion in the following sections.

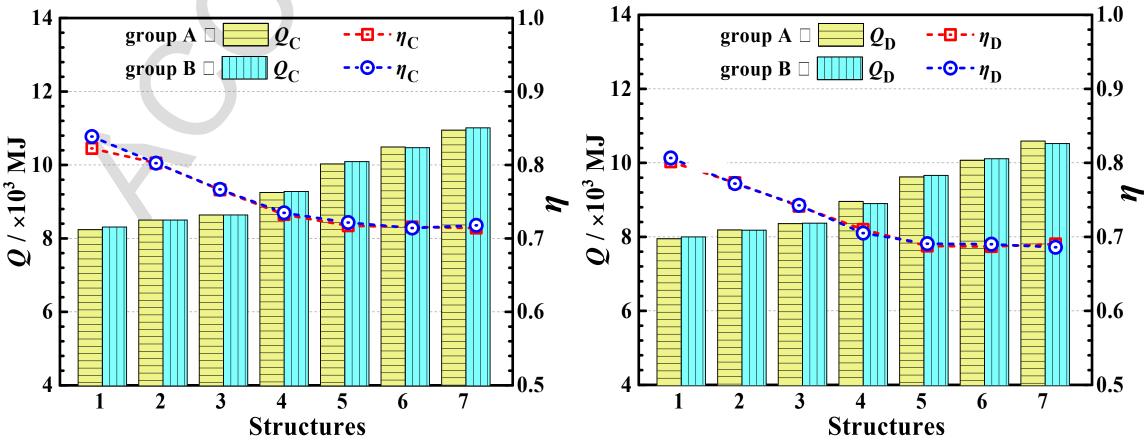

(a) Charging (b) Discharging

Fig. 13. Comparison of the thermal performance of group A and group B in a period cycle.

The cost analysis is conducted using more realistic large-scale tanks rather than the small-scale tanks studied above. The large-scale tanks are all assumed to have the Q_D of 100 MWht. It is known that the thermal efficiencies of a thermocline tank are affected by the tank height, but they are barely affected by the tank diameter. Therefore, the heights of the large-scale tanks are assumed be the same as that of the small-scale tanks, and the efficiency data obtained in previous study is employed in the cost analysis. Meanwhile, the diameters are adjusted to ensure that Q_D=100 MWht.

Table 6 shows the capital costs of large-scale (Q_D=100 MWht) SLPBTTs and MLPBTTs as described in Section 2.3. First, it is seen in Table 6 that the C_{TES} of SLPBTT using quartzite rock is the lowest among the single-layer structures because of its low price and relatively high efficiency. Besides, the experiment has proved that the quartzite rock held up remarkable thermal performance after 553 cycles in the Sandia National Laboratories [23]. So the characteristics of quartzite rock including low price, high efficiency and good thermal stability made the quartzite rock be chosen as the best filler material for SLPBTT in the present work. SLPBTT using the quartzite rock will be taken as the typical SLPBTT for further discussion in the following sections. Second, the C_{TES} of SLPBTT adopting cast iron is much higher than those of other structures, so the SLPBTT using cast iron is not suitable for the industrial application despite its large volumetric heat capacity. Moreover, the filler cost of MLPBTT increases from structure A-1 to A-7 due to the increment of the expensive cast iron, but the container cost decreases due to the decrement of the tank's volume. Finally, it is found that the C_{TES} of MLPBTT increases from structure A-1 to A-7.

Table 6 Capital costs of SLPBTTs and MLPBTTs for a 100 MWht thermocline storage tank.

Structures	Cost for per \$ kWht^{-1}			Capital cost C_{TES} / \$ kWht^{-1}
	Fillers	Container	Purchased equipment	
S-quartzite	0.6	21.6	38.7	60.9
S-iron	22.8	11.7	38.7	73.2
S-concrete	4.0	19.1	38.7	61.8
A-1	2.1	20.6	38.7	61.4
A-2	4.5	19.9	38.7	63.1
A-4	6.8	19.3	38.7	64.8
A-5	10.5	18.2	38.7	67.4
A-6	13.7	17.2	38.7	69.6
A-7	14.8	16.6	38.7	70.1
A-8	15.6	15.9	38.7	70.2

Fig. 14 shows the thermal performance (Q_C, Q_D, η_C, η_D) and capital cost (C_{TES}) of three SLPBTTs and seven MLPBTTs in a period cycle. First, in group A of Fig. 14, the useful thermal energy (Q_C, Q_D) increase from structure A-1 to A-7 with increasing cast iron's height (H_{ci}) due to large $\rho_s c_{p,s}$ of it. For example, in a periodic discharging process in Fig. 14, Q_D for A-1 with H_{ci} =0 m is just 7.95×10^3 MJ, and Q_D for A-6 with H_{ci} =2.1 m is 9.62×10^3 MJ. However, the efficiencies (η_C, η_D) decrease with increasing H_{ci} except those of A-1 with H_{ci}=0. It is seen that η_C and η_D decrease sharply from A-1 to A-4, whereas η_C and η_D remain approximately at 72% and 69%, respectively, from A-5 to A-7.

In addition, by comparing the performance of group A with that of SLPBTT using quartzite rock, it is seen that the stored useful energy can be effectively improved with a small drop in thermal efficiency when cast iron is relatively thin. For example, an increase in Q_D of 10.5% and a drop in η_D of 2.1 % for structure A-2 can be observed compared with that of SLPBTT using quartzite rock. However, when cast iron is relatively thick, even though Q_C and Q_D are improved significantly, η_C and η_D are reduced importantly. For example, a rise in Q_D of 35.9% and a large drop in η_D of 10.7% for structure A-6 are observed compared with that of SLPBTT using quartzite rock. Meanwhile, comparing with that of SLPBTT using cast iron, the η_D of A-1 and A-2 can be improved by 11.2 % and 8.3 %, respectively, and the C_{TES} of A-1 and A-2 can be significantly reduced by 16.2 % and 14.0 %, respectively. From current results, the structure of MLPBTT with small H_{ci} is recommended to achieve a high efficiency, reasonable useful large thermal energy and low capital cost, e.g., structure A-1and A-2.

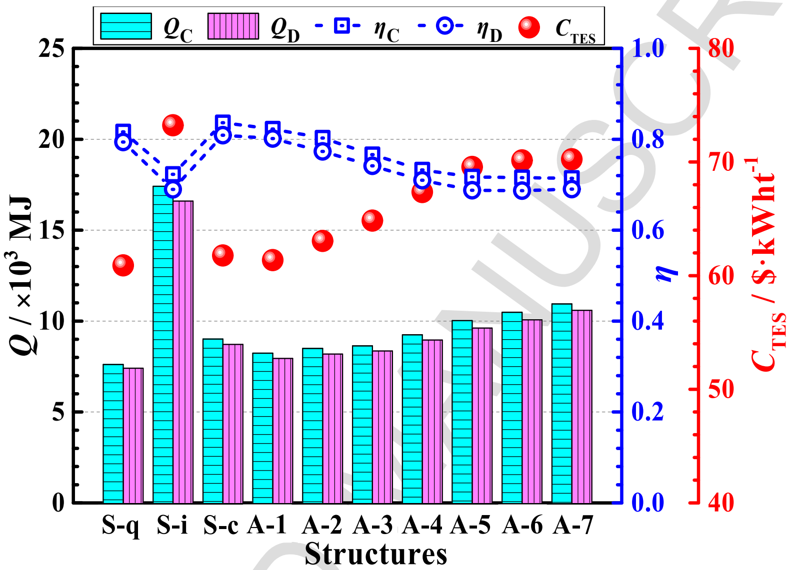

Fig. 14. Comparison of the thermal performance and capital cost of SLPBTTs and MLPBTTs in a period cycle.

4.3.3 Effect of thermocline on thermal performance

Fig. 15 shows the development of thermocline thickness for seven structures in group A and SLPBTT using quartzite rock. From Fig. 15 (a), it can be seen that L of structures SLPBTT and A-1, without cast iron, is relatively small with the maximum thermocline thickness L_{max}<2.8m in the charging process. However, once the cast iron is added, L_{max} will become much larger due to the expanding effect at the interface between cast iron and quartzite rock, e.g., A-2 to A-7.

From Fig. 15 (b), it is seen that L of SLPBTT, and A-1 to A-3 increases at the beginning of a discharging process due to the thermocline region expansion in quartzite rock. However, no improvement of L is observed for other structures (A-4 to A-7) due to the shortening effect at the interface of quartzite rock and cast iron, where the thickness of retention thermocline in the previous charging cycle is larger than the filling height of quartzite rock (H_{qr}).

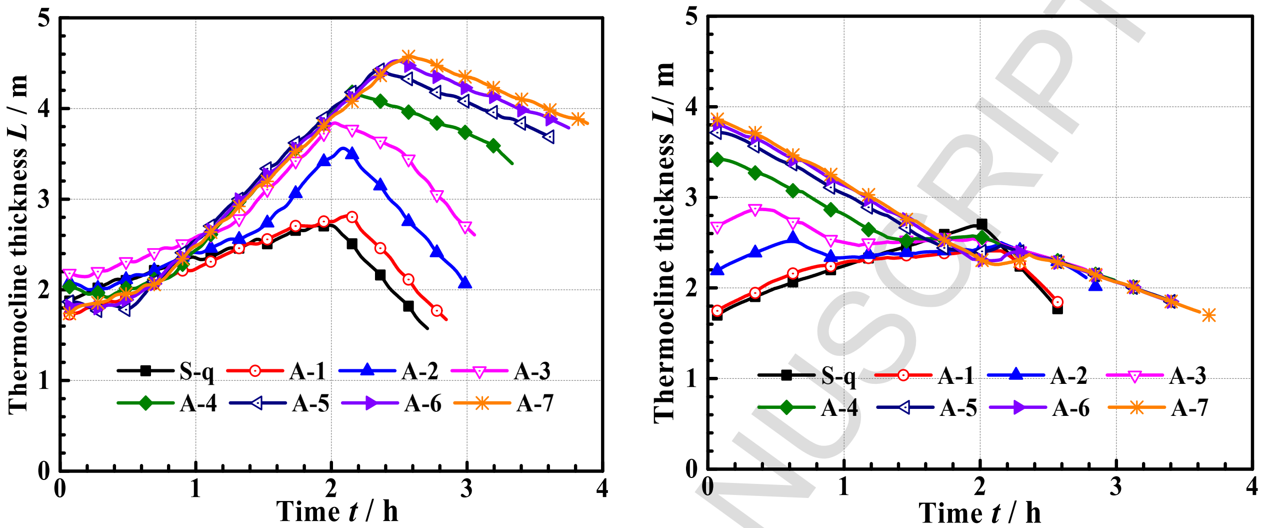

(a) Charging (b) Discharging

Fig. 15 Comparison on thermocline thicknesses at different structures in a period cycle.

Fig. 16 shows the retention thermocline thickness of different structures in a periodic cycle, where the filling heights of three fillers are also illustrated. It is seen that the thickness of the retention thermocline for charging ($L_{R,C}$) rises with the increasing H_{ci}. It is mainly due to the increasing time for crossing the interface between cast iron and quartzite rock as shown in Fig. 15 (a), which is caused by the expanding effect at this interface. However, the thickness of the retention thermocline for discharging ($L_{R,D}$) process firstly increases and then decreases with the improvement of H_{ci} from A-1 to A-7. This is because of the combined influence of the shortening effect between quartzite rock and cast iron, and the expanding effect between cast iron and concrete.

In addition, it can be concluded that η_D of A-4 (71.0%) is much less than that of A-2 (77.3%), even though $L_{R,D}$ of A-4 (2.0m) is similar to that of A-2 (2.1m) in Fig. 16 and Fig. 14 (b) . It is seen that the retention thermocline region is within the region of Concrete for A-2 as well, but, it covers both concrete and cast iron for A-4. Because a lot of thermal energy stored in cast iron where volumetric heat capacity is the largest among fillers for the A-4 cannot be adequately unitized. These results indicate that the thermal performance of MLPBTT is not only related to the thickness of retention thermocline (L_R), but also closely related the relation of L_R and filling height of filler. From above results, it is recommended that the retention thermocline thickness for present three-layered PBTT should follow the relation in Eq. (25) for achieving a relatively high efficiency. Therefore, the structure A-2 without retention thermocline in the cast iron is recommended.

$$L_{R,C} \le H_{qr} \quad \text{and} \quad L_{R,D} \le H_{hc} \tag{25}$$

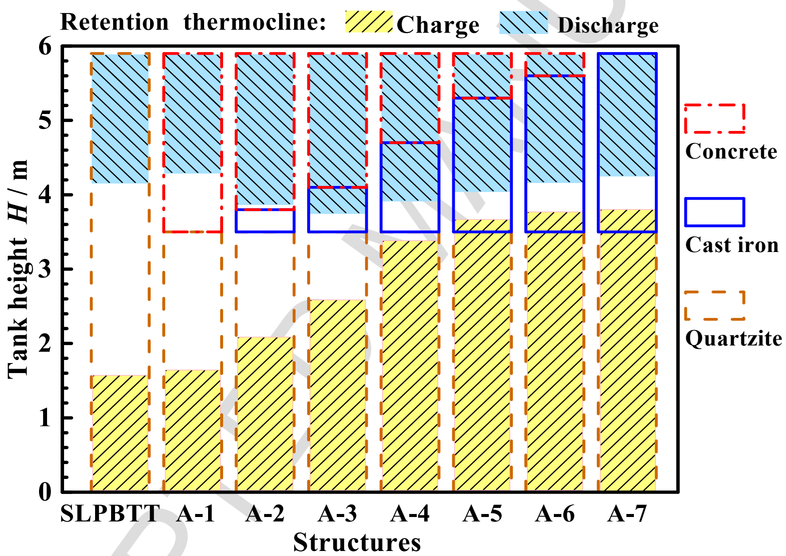

Fig. 16 Relations of retention thermocline region and filler heights for the structures in a periodic cycle.

5. Conclusions

In the work, cyclic thermal performance of a traditional Single-Layered and of a novel Multi-Layered Packed-Bed molten salt Thermocline Tank (SLPBTT, MLPBTT) was studied. The following conclusions could be derived.

(1) The analysis of the cyclic thermal performance of SLPBTT and the effect of thermocline indicates that the following items, including the stored thermal energy (Q_C), the released thermal

energy (Q_D), the charging efficiency (η_C), and the discharging efficiency (η_D), can be increased by reducing the retention thermocline thickness (L_R).

(2) The interface effect on thermocline, which refers to the expanding or shortening effect at the interface between two kinds of filler on thermocline thickness, is first reported. When salt flows from one filler with a slower expanding velocity of thermocline to another one with a fast expanding velocity, thermocline thickness will be increased, and vice versa. It is suggested that the thermocline development can be controlled by utilizing the interface effect in the MLPBTT, which is filled with different fillers orderly.

(3) Study on the performance of MLPBTTs designed by utilizing the interface effect presents that Q_C, Q_D can be increased while η_C, η_C will be reduced with the increasing cast iron's height (H_{ci}) in the MLPBTT. It is also found that the retention thermocline for present MLPBTT should not stay at the cast iron region for achieving a relatively high efficiency.

(4) The optimization of the MLPBTT shows that the stored useful energy can be significantly improved with a small drop in thermal efficiency compared with those of SLPBTT using quartzite rock. A rise in discharging useful energy of 10.5% and a drop in discharging efficiency of 2.1 % can be observed for this MLPBTT in which the filling heights of quartzite rock, cast iron, and high-temperature concrete are 3.5m, 0.3m, and 2.1m, respectively.

In conclusion, results can be useful to provide guidance of the further design and performance optimization of packed-bed thermocline thermal storage tanks.

Acknowledgements

The study is supported by the National Key R&D Program of China (2017YFB0601801) and the Key Project of National Science Foundation of China (No.51436007).

The authors would also like to thank the Innovative Talents Support Plan of China Postdoctoral Foundation (BX201700189).

Nomenclature

C_2	inertial coefficient
C_{TES}	the total capital cost of the thermocline TES ($)
$C_{\mathrm{TES,total}}$	the capital cost of the thermocline TES ($\$\cdot$kWht^{-1})
c_{p}	specific heat capacity (J·kg^{-1}·K^{-1})
D	diameter of packed-bed region (m)
d_{p}	diameter of the particle filler (m)
g	acceleration due to gravity (m·s^{-2})
H	height of packed-bed region (m)
h	heat transfer coefficient (W·m^{-2}·K^{-1})
h_V	volumetric interstitial heat transfer coefficient (W·m^{-3}·K^{-1})
K	permeability
k	thermal conductivity (W·m^{-1}·K^{-1})
L	thermocline thickness (m)
L_{R}	retention thermocline thickness (m)
l	thickness (m)
Pr	Prandtl number
p	pressure (Pa)
Q	thermal energy (J)
Q_{ideal}	the maximum thermal energy stored in a tank (J)
Q	thermal power (W)
Re	Reynolds number
r	radius (m)
T	temperature (°C)
T_{h}	critical high temperature of thermocline region (°C)
T_{l}	critical low temperature of thermocline region (°C)
t	time (h)
u	velocity (m·s^{-1})

x	location along the axis of the tank (m)
Greek symbols	
ε	porosity of packed-bed region
η	thermal efficiency
μ	viscosity ($kg{\cdot}m^{-1}{\cdot}s^{-1}$)
ρ	density ($kg{\cdot}m^{-3}$)
Subscripts	
air	ambient air
C, D	charging / discharging parameter
ci	cast iron
eff	effective
f	fluid
hc	high- temperature concrete
in, out	inlet / outlet parameter
in1	inside insulation layer
in2	outside insulation layer
loss	heat loss
qr	quartzite rock
s	solid filler material
st	stainless steel
th	threshold value

References

[1] Khare V, Nema S, Baredar P. Solar–wind hybrid renewable energy system: A review. Renewable and Sustainable Energy Reviews. 2016;58:23-33.

[2] Yan J. Handbook of Clean Energy Systems2015.

[3] Li M-J, He Y-L, Tao W-Q. Modeling a hybrid methodology for evaluating and forecasting regional energy efficiency in China. Applied Energy. 2017;185:1769-77.

[4] Li M-J, Zhao W, Chen X, Tao W-Q. Economic analysis of a new class of vanadium redox-flow battery for medium- and large-scale energy storage in commercial applications with renewable energy. Applied Thermal Engineering. 2017;114:802-14.

[5] Li M-J, Song C-X, Tao W-Q. A hybrid model for explaining the short-term dynamics of energy efficiency of China's thermal power plants. Applied Energy. 2016;169:738-47.

[6] Hosseini SE, Wahid MA. Hydrogen production from renewable and sustainable energy resources: Promising green energy carrier for clean development. Renewable and Sustainable Energy Reviews. 2016;57:850-66.

[7] Li M-J, Tao W-Q. Review of methodologies and polices for evaluation of energy efficiency in high energy-consuming industry. Applied Energy. 2017;187:203-15.

[8] Qiu Y, Li M-J, He Y-L, Tao W-Q. Thermal performance analysis of a parabolic trough solar collector using supercritical CO 2 as heat transfer fluid under non-uniform solar flux. Applied Thermal Engineering. 2017;115:1255-65.

[9] He Y-L, Zheng Z-J, Du B-C, Wang K, Qiu Y. Experimental investigation on turbulent heat transfer characteristics of molten salt in a shell-and-tube heat exchanger. Applied Thermal Engineering. 2016;108:1206-13.

[10] Qiu Y, He Y-L, Wu M, Zheng Z-J. A comprehensive model for optical and thermal characterization of a linear Fresnel solar reflector with a trapezoidal cavity receiver. Renewable Energy. 2016;97:129-44.

[11] Qiu Y, He Y-L, Cheng Z-D, Wang K. Study on optical and thermal performance of a linear Fresnel solar reflector using molten salt as HTF with MCRT and FVM methods. Applied Energy. 2015;146:162-73.

[12] Fuqiang W, Qingzhi L, Huaizhi H, Jianyu T. Parabolic trough receiver with corrugated tube for improving heat transfer and thermal deformation characteristics. Applied Energy. 2016;164:411-24.

[13] Ma Z, Yang W-W, Yuan F, Jin B, He Y-L. Investigation on the thermal performance of a high-temperature latent heat storage system. Applied Thermal Engineering. 2017;122:579-92.

[14] Wu M, Xu C, He Y. Cyclic behaviors of the molten-salt packed-bed thermal storage system filled with cascaded phase change material capsules. Applied Thermal Engineering. 2016;93:1061-73.

[15] Tao YB, He YL. Effects of natural convection on latent heat storage performance of salt in a horizontal concentric tube. Applied Energy. 2015;143:38-46.

[16] Xu Y, He Y-L, Li Y-Q, Song H-J. Exergy analysis and optimization of charging–discharging processes of latent heat thermal energy storage system with three phase change materials. Solar Energy. 2016;123:206-16.

[17] Xu Y, Ren Q, Zheng Z-J, He Y-L. Evaluation and optimization of melting performance for a latent heat thermal energy storage unit partially filled with porous media. Applied Energy. 2017;193:84-95.

[18] Zhang P, Xiao X, Ma ZW. A review of the composite phase change materials: Fabrication, characterization, mathematical modeling and application to performance enhancement. Applied Energy. 2016;165:472-510.

[19] Qiu Y, He Y-L, Li P, Du B-C. A comprehensive model for analysis of real-time optical performance of a solar power tower with a multi-tube cavity receiver. Applied Energy. 2017;185:589-603.

[20] Nallusamy N, Sampath S, Velraj R. Experimental investigation on a combined sensible and latent heat storage system integrated with constant/varying (solar) heat sources. Renewable Energy. 2007;32:1206-27.

[21] Lu J, Yu T, Ding J, Yuan Y. Thermal storage performance of molten salt thermocline system with packed phase change bed. Energy Conversion and Management. 2015;102:267-74.

[22] Libby C. Solar Thermocline Storage System: Preliminary Design Study. In: 1019581, editor. Electric Power Research Institute, Palo Alto, CA2010. p. 1019581.

[23] Pacheco JE, Showalter SK, Kolb WJ. Development of a molten-salt thermocline thermal storage system for parabolic trough plants. Journal of solar energy engineering. 2002;124:153-9.

[24] Okello D, Nydal OJ, Nyeinga K, Banda EJ. Experimental investigation on heat extraction from a rock bed heat storage system for high temperature applications. Journal of Energy in Southern Africa. 2016;27:30-7.

[25] Okello D, Foong CW, Nydal OJ, Banda EJK. An experimental investigation on the combined use of phase change material and rock particles for high temperature (~350°C) heat storage. Energy Conversion and Management. 2014;79:1-8.

[26] Okello D, Nydal OJ, Banda EJK. Experimental investigation of thermal de-stratification in rock bed TES systems for high temperature applications. Energy Conversion and Management. 2014;86:125-31.

[27] Zanganeh G, Pedretti A, Zavattoni S, Barbato M, Steinfeld A. Packed-bed thermal storage for concentrated solar power – Pilot-scale demonstration and industrial-scale design. Solar Energy. 2012;86:3084-98.

[28] Li Q, Bai F, Yang B, Wang Z, El Hefni B, Liu S, et al. Dynamic simulation and experimental validation of an open air receiver and a thermal energy storage system for solar thermal power plant. Applied Energy. 2016;178:281-93.
[29] Bruch A, Fourmigué JF, Couturier R. Experimental and numerical investigation of a pilot-scale thermal oil packed bed thermal storage system for CSP power plant. Solar Energy. 2014;105:116-25.
[30] Vaivudh S, Rakwichian W, Chindaruksa S. Heat transfer of high thermal energy storage with heat exchanger for solar trough power plant. Energy Conversion and Management. 2008;49:3311-7.
[31] Grirate H, Agalit H, Zari N, Elmchaouri A, Molina S, Couturier R. Experimental and numerical investigation of potential filler materials for thermal oil thermocline storage. Solar Energy. 2016;131:260-74.
[32] Xu C, Li X, Wang Z, He Y, Bai F. Effects of solid particle properties on the thermal performance of a packed-bed molten-salt thermocline thermal storage system. Applied Thermal Engineering. 2013;57:69-80.
[33] Xu C, Wang Z, He Y, Li X, Bai F. Sensitivity analysis of the numerical study on the thermal performance of a packed-bed molten salt thermocline thermal storage system. Applied Energy. 2012;92:65-75.
[34] Bayón R, Rojas E. Analytical Description of Thermocline Tank Performance in Dynamic Processes and Stand-by Periods. Energy Procedia. 2014;57:617-26.
[35] Bayón R, Rivas E, Rojas E. Study of Thermocline Tank Performance in Dynamic Processes and Stand-by Periods with an Analytical Function. Energy Procedia. 2014;49:725-34.
[36] Mawire A, McPherson M. Experimental characterisation of a thermal energy storage system using temperature and power controlled charging. Renewable Energy. 2008;33:682-93.
[37] Hoffmann JF, Fasquelle T, Goetz V, Py X. A thermocline thermal energy storage system with filler materials for concentrated solar power plants: Experimental data and numerical model sensitivity to different experimental tank scales. Applied Thermal Engineering. 2016;100:753-61.
[38] Xu B, Li P, Chan CL. Energy Storage Start-up Strategies for Concentrated Solar Power Plants With a Dual-Media Thermal Storage System. Journal of Solar Energy Engineering. 2015;137:051002--12.
[39] Zanganeh G, Pedretti A, Haselbacher A, Steinfeld A. Design of packed bed thermal energy storage systems for high-temperature industrial process heat. Applied Energy. 2015;137:812-22.
[40] Galione PA, Pérez-Segarra CD, Rodríguez I, Oliva A, Rigola J. Multi-layered solid-PCM thermocline thermal storage concept for CSP plants. Numerical analysis and perspectives. Applied Energy. 2015;142:337-51.
[41] Klein P, Roos TH, Sheer TJ. Parametric analysis of a high temperature packed bed thermal storage design for a solar gas turbine. Solar Energy. 2015;118:59-73.
[42] Zavoico A. Solar Power Tower Design Basis Document. Sandia National Laboratories 2001. Report no SAND2001-2100.
[43] W.Q. Tao, Numerical Heat Transfer, second ed., Xi'an Jiaotong University Press,Xi'an, 2001.
[44] ANSYS FLUENT 14.0 Theory Guide, ANSYS Inc, 2011.
[45] Alazmi B, Vafai K. Analysis of variants within the porous media transport models. Journal of Heat Transfer. 2000;122:303-26.
[46] Ismail K, Stuginsky Jr R. A parametric study on possible fixed bed models for pcm and sensible heat storage. Applied Thermal Engineering. 1999;19:757-88.
[47] Strasser MN, Selvam RP. A cost and performance comparison of packed bed and structured thermocline thermal energy storage systems. Solar Energy. 2014;108:390-402.
[48] Zhao BC, Cheng MS, Liu C, Dai ZM. Thermal performance and cost analysis of a multi-layered solid-PCM thermocline thermal energy storage for CSP tower plants. Applied Energy. 2016;178:784-99.

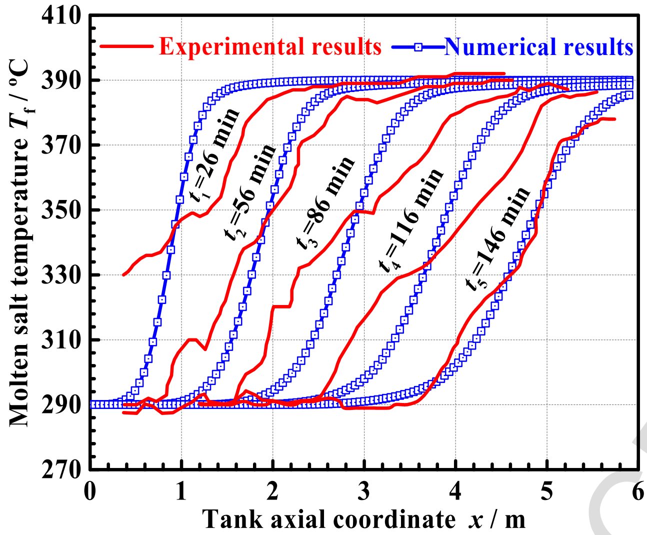

Fig. 5 Comparison between present numerical result of the axial molten salt temperature and the experimental results from Pacheco et al. [23].

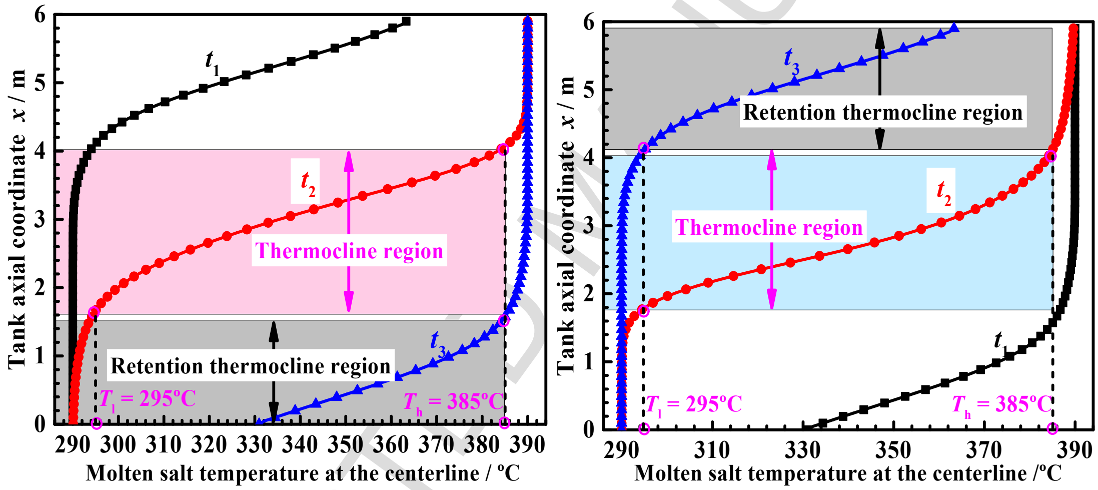

(a) Charging (b) Discharging

Fig. 7 Axial temperature distributions of salt at t_1=0 h, t_2=1.2 h and t_3=t_D or t_C in the periodic state.

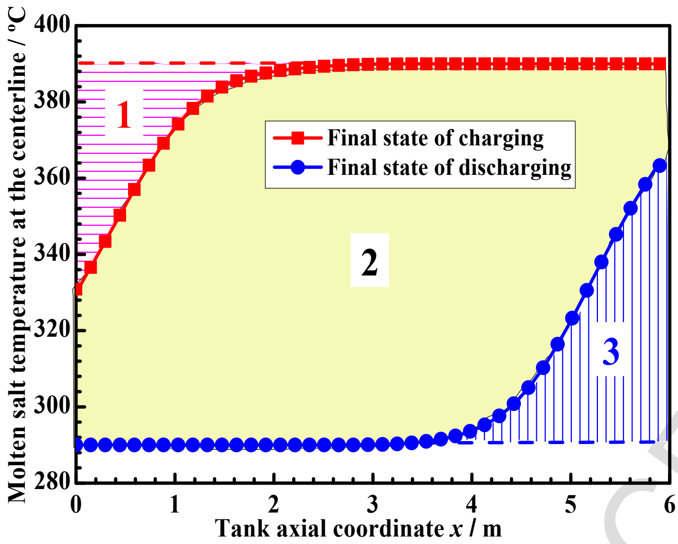

Fig. 9 Axial temperatures of salt at final state of charging and discharging processes at periodic cycle.